Supplementary Materials

Operando X-ray scattering reveals ordering-mediated solidification in additive manufacturing

Lin Gao[1,3,*], Kyle Mumm[2], Zhongshu Ren[1,2#], Zhou Yu[3], Xingyang Li[2], Andrew C. Chuang[4], Tao Sun[1,2,*]

[1]Department of Materials Science and Engineering, University of Virginia; Charlottesville, VA, USA

[2]Department of Mechanical Engineering, Northwestern University; Evanston, IL, USA

[3]Department of Mechanical Engineering, The University of Alabama; Tuscaloosa, AL, USA

[4]X-ray Science Division, Argonne National Laboratory; Lemont, IL, USA

[*]Corresponding authors. Emails: lgao9@ua.edu (LG), taosun@northwestern.edu (TS)

[#]Current address: National Synchrotron Light Source II, Brookhaven National Laboratory; Upton, NY, USA

The PDF file includes:

1. Materials and Methods

1.1 Wire-laser directed energy deposition process

Wire-laser directed energy deposition (DED) was performed using two commercial systems: μPrinter (Additec, USA) and M450 (Meltio, Spain). The μPrinter featured a triple-laser configuration and was modified for *operando* synchrotron experiments. All bulk samples studied in this work were fabricated using the M450 printer, which was equipped with six laser sources and offered better productivity for manufacturing large-scale samples. The printheads in these DED systems have similar configurations: the laser beams were focused centrosymmetrically on a wire feedstock delivered through the center of the stationary printhead. The deposition process was realized by scanning the built platform. The key printing parameters used in this study are listed in Table S1. The linear energy density (LED) and volumetric energy density (VED) reported in the main text were calculated using the expressions $LED = P/V$ and $VED = P/A/F$, where P, V, A, and F refer to the laser power, scanning speed, cross-sectional area of wire feedstock, and feeding rate, respectively.

Table S1. Printing parameters used in this study. All wire feedstocks had a diameter of 0.9 mm.

Materials	Condition	Sample type	Power (W)	Scanning speed($mm \cdot s^{-1}$)	Feeding rate ($mm \cdot s^{-1}$)
Inconel 718	Transitional (R)	Single track	600.0	5.8	29.0
Inconel 718	Lack of Fusion	Single track	400.0	10.0	17.0
Inconel 718	Normal	Single track	600.0	6.7	11.4
Inconel 718	Transitional	Bulk	1000.0	16.7	83.3
316L	Transitional	Single track	400.0	7.0	7.7
Pure Ni	Normal	Single track	600	6.7	11.4

1.2 Ex-situ microstructure characterization

Samples for postmortem characterization were sectioned using wire electrical discharge machining (EDM). The sample surfaces were mechanically ground using sandpapers of progressively finer grits, followed by sequential polishing with diamond suspensions and a final polish using a colloidal silica suspension. Scanning electron microscopy (SEM) was conducted using a Helios UC G4 dual-beam SEM equipped with an Oxford electron backscatter diffraction (EBSD) detector. Post data analysis was performed using the software *Aztec Crystal*. Metallographic analysis was performed using a Hirox digital light microscope. Prior to imaging, samples were electrolytically etched in a 10% oxalic acid solution at 3 V.

1.3 *Operando* synchrotron X-ray experiment

Operando synchrotron X-ray experiments were conducted at the 1-ID-E beamline of Advanced Photon Source (APS), Argonne National Laboratory. A superconducting undulator generated high-energy flux and a monochromator was used to select X-rays with energy of 100.0 keV. Full-field imaging was carried out using a Pointgrey GS3-U3-23S6M-C CMOS camera, a 5× objective lens, and a 25 μm-thick LuAG:Ce scintillator, achieving a pixel resolution of 1.172 μm and a frame rate of 80 Hz. For diffraction characterization, the X-ray beam was focused using a series of compound refractive lenses and then collimated using slits into a 50 μm (width) × 30 μm (height) rectangular shape. A PILATUS3X CdTe 2M detector was mounted downstream to

continuously capture 2D diffraction patterns at a frame rate of 250 Hz with an exposure time of 3 ms for each frame. High-flux, high-energy X-rays combined with an efficient detector featuring high dynamic range and zero noise are essential for capturing diffraction patterns over a large *q*-range. This capability is critical for total-scattering measurements of liquid metals. Figure S1 presents photographs of our *operando* characterization setup at the 1-ID-E beamline of the APS.

In the synchrotron experiment, the printing process was carried out using the µPrinter. Because the track deposition was achieved by translating the build platform instead of the printhead, the X-ray beam could be set at a specific location in the melt pool, enabling the collection of diffraction data from the same material state for a relatively long time (on the order of seconds, depending on the track length). This Eulerian reference frame facilitates in-depth analyses of melt pool structures and dynamics, in statistically averaged and time-resolved manners. Individual diffraction patterns collected at 250 Hz provide valuable insights into transient melt pool phenomena. At the same time, diffraction data acquired from the same melt pool position can be summed to generate a high-quality pattern that encodes structural information with improved statistics. Systematically repositioning the X-ray beam and repeating the diffraction measurements allow tracking of microstructural evolution during the DED process. More details on the experiment and data interpretation are included in our prior publication, which focused on studying the solid-state transformation during the cooling stage in the wire-laser DED process[17].

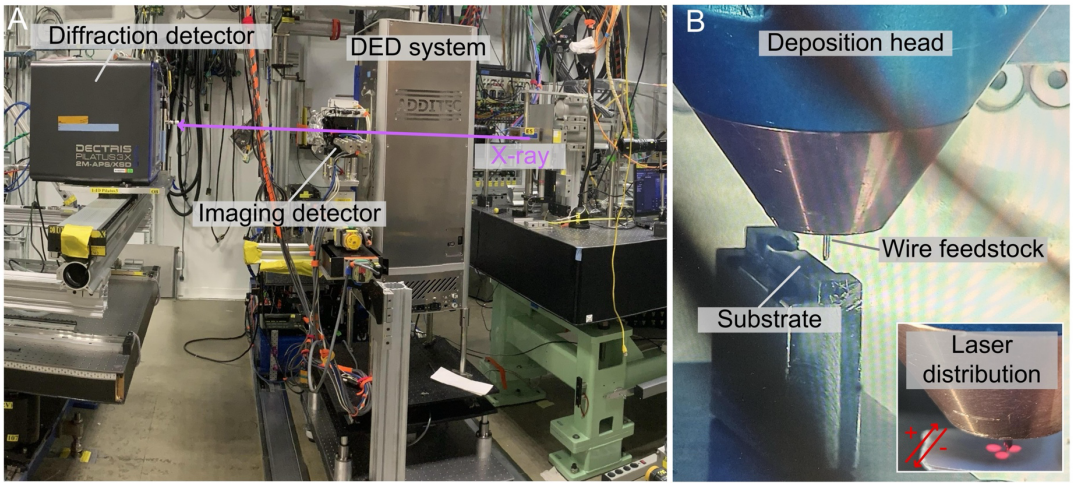

Fig. S1. Photographs of *operando* synchrotron experiment at the 1-ID-E beamline of the Advanced Photon Source, Argonne National Laboratory. (A) The wire-laser DED system along with key X-ray instruments at the beamline. **(B)** The printhead of DED system and the sample substrate. The inset shows the arrangement of the three coaxial lasers surrounding the wire (indicated by the Class I red guide lasers). The positive (+) and negative (-) deposition directions are indicated by the two red arrows.

1.4 Total-scattering structure function and pair distribution function analysis

The time-resolved X-ray diffraction patterns collected at each specific location underwent the following steps for total scattering and pair distribution function analyses.

1) For each individual measurement with the X-ray probing at a specific location, diffraction patterns corresponding to the stable printing period (i.e. excluding the initial and final stages of the laser deposition) were picked out from the entire sequence (330 frames out of 2000 frames). These patterns were summed and integrated into a one-dimensional (1-D) profile across the entire

Azimuth range using the software *GSAS II*[41]. Instrumental parameters employed in the integration and subsequent analysis were calibrated using a standard CeO_2 powder sample. This procedure was repeated for other batches of data collected from different locations and other printing processes/materials.

2) Each 1-D scattering profile was processed using *PDFGetX2* software for background correction and pair distribution function (PDF) profile extraction[42]. The measured 1-D scattering profile included signals from the sample, air, and two laser-protective glass windows on the DED chamber, positioned in front of and behind the sample. Background signals from these components were individually measured by several static diffraction experiments (off-laser) with and without these laser-protective glasses, which were then subtracted from the measured 1D scattering profile. The attenuation effect of the thick metal sample on background signals was accounted for via the attenuation coefficient

$$\frac{I(z)}{I_0} = e^{-(\rho \sum_j w_j \mu_j) z}$$

where ρ, w_j, μ_j, and z are the density of Inconel 718, mass fraction of element j, mass attenuation of element j, and the sample thickness, respectively.

3) Following background correction, the 1D scattering intensity profile *I(Q)* was converted to the total-scattering structure function *S(Q)* and reduced pair distribution function *G(r)*. These conversions from *I(Q)* to *S(Q)* and *G(r)* were carried out using *PDFgetX2* software based on the following mathematics:

$$S(Q) = \frac{I(Q)}{\langle b \rangle^2}$$

$$G(r) = \frac{2}{\pi} \int_0^\infty Q[S(Q) - 1] \sin(Qr) dQ$$

where $\langle b \rangle$ indicates the compositional average of the atomic scattering amplitude. The range of wavevector Q used for the PDF extraction was from 0.82 to 14.82 $Å^{-1}$.

Figure S2 shows a batch of *I(Q)* profiles integrated from individual patterns within a data sequence. The profiles exhibit no significant variation, confirming the feasibility of summing these data sequences corresponding to the steady-state printing period for further analysis. Moreover, each single *I(Q)* profile presents a relatively low signal-to-noise ratio, underscoring the necessity of our Eulerian reference configuration to obtain high-quality PDF data.

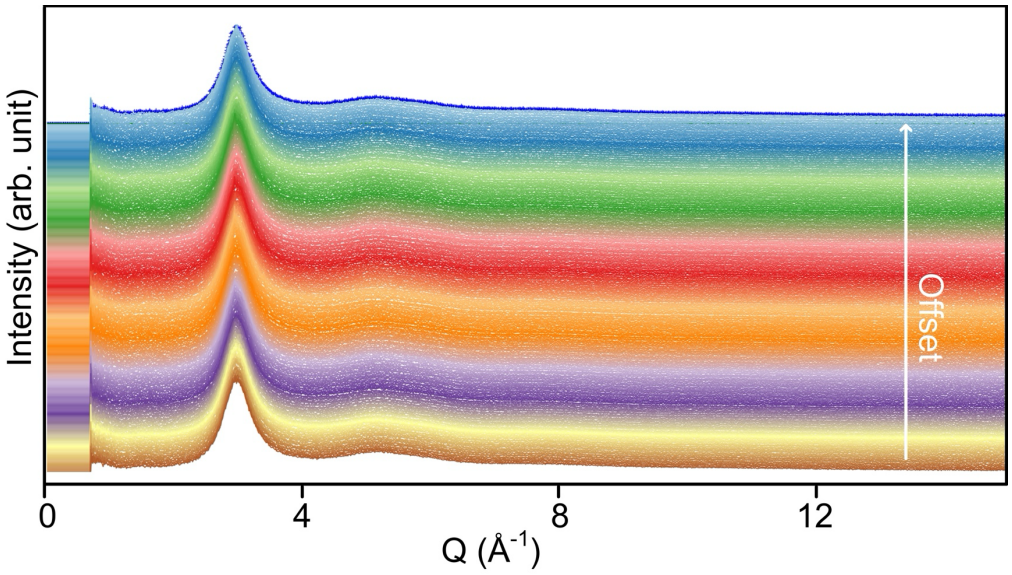

Fig. S2. I(Q) profiles obtained from a sequence of time-resolved scattering patterns. Each profile was integrated from an individual 2D diffraction pattern in a dataset, yielding a total of 330 profiles, shown with color distinction and vertical offsets. Each profile corresponds to a 4 ms time interval (3 ms exposure + 1 ms dwell time), reflecting the instantaneous melt pool structure. In our PDF analysis, these individual diffraction intensities were summed together to yield a single profile with a much higher signal-to-noise ratio.

1.5 Small-box fitting of PDF profiles

Each extracted PDF profile, *G(r)*, was imported into the software *PDFgui* for small-box fitting[43]. The atomic models presented in Fig. 2e of the main text were utilized for fitting. Parameters, including the isotropic Gaussian atomic displacement parameter (ADP), scale factor, linear atomic correlation factor δ_1, and lattice parameters, were refined for each phase and atomic clusters within an *r* range of 1 - 80 Å. The fraction and atomic displacement of each structure illustrated in Fig. 3 were calculated based on the refined scale factors and lattice parameters, respectively.

Both the FCC solid and FCC-like atomic clusters were fitted using crystal models with the $Fm\bar{3}m$ space group. In comparison, the FCC-like atomic cluster, due to its amorphous nature, exhibited a notably higher ADP value and a size parameter *spdiameter*. Consequently, the increased ADP and size effects manifested as significant peak broadening and diminished oscillation amplitude with increasing *r* in the *G(r)* profiles.

Because five-fold symmetry cannot be described by conventional space groups, the fitting method applied to FCC-like clusters is not applicable to icosahedral clusters. To address this issue in small-box fitting, a cubic supercell encompassing an entire icosahedral cluster was constructed following the method suggested by Chen et al.[44]. The packing density of the cluster was corrected using a composite modeling approach elaborated in the referenced study. Within this configuration, the size of the clusters with icosahedral medium-range order (IMRO) was not refined by the size parameter *spdiameter*; instead, various sizes were manually tested to achieve the most optimized fitting. The cluster size was adjusted by adding or removing outer-shell layers according to the Mackay growth mode for icosahedral ordering, which was implemented using MATLAB code[45]. The IMRO also exhibited broadened peaks due to its liquid nature, but it could be distinguished from FCC-like clusters by differing peak positions. In contrast, the icosahedral short-range order

(ISRO), containing only 13 atoms, represented more randomly arranged atoms in the liquid phase with larger interatomic separations. Refinement of the ISRO was conducted as the final step of the PDF analysis, with this structure constituting only a minor fraction of all fitted phases and liquid clusters.

It is important to emphasize that this refinement focused solely on topological orderings, as chemical ordering was considered to have minimal impact on *G(r)*, given the nearly identical scattering cross-sections of the primary elements in Inconel 718 when probed by high-energy X-rays, where $f_{1,Fe}$ = 26.0 e/atom; $f_{1,Ni}$ = 28.1 e/atom; and $f_{1,Cr}$ = 24.0 e/atom[46]. Another source of uncertainty arises from crystallographic texture in solidified columnar grains, particularly pronounced under the Normal printing condition, where preferred orientation slightly affects the relative intensities of specific peaks. Therefore, PDF refinement was not performed for the late solidification stage. The resulting model agreement scores for all refinements fell within the range of $8.0\% < Rw < 15.1\%$, indicating robust reliability and appropriate model selection in the present analysis. Here, *Rw* denotes the standard deviation between the fitted and experimental profiles. Error bars for the fraction of each fitted structure were calculated based on a 10% deviation from the corresponding *Rw* values.

1.6 Correlograph analysis of time-resolved diffraction

The correlograph analysis was performed for individual diffraction patterns. As mentioned in the earlier section, the Eulerian reference setup of our *operando* characterization enabled monitoring of the dynamic evolution of melt pool microstructures during the stable printing process. With X-rays probing the mushy zone, each diffraction frame captured a transient moment of the solidification front, potentially revealing statistical geometry relationships among primarily solidified grains through correlograph analysis. This method was previously developed and successfully applied to identify the local symmetries in disordered materials based on X-ray or electron diffraction patterns[47,48].

In our analysis, $(200)_{FCC}$ diffraction was integrated over the entire azimuth range in a step size of 1° in $\Delta\Phi$. Each diffraction pattern yielded a diffraction intensity profile as a function of the azimuth angle, $I(\Phi)$. Subsequently, the normalized angular correlation function was applied to the profile:

$$C(\Delta\Phi) = \frac{\langle I(\Phi)I(\Phi+\Delta\Phi)\rangle_{\Phi} - \langle I(\Phi)\rangle_{\Phi}^{2}}{\langle I(\Phi)\rangle_{\Phi}^{2}}$$

where $\Delta\Phi$ is the variable of angular offset, and the $\langle\ \rangle$ operation was applied to a uniform averaging over all azimuth angles from 0 to 360°. This analysis was carried out sequentially over 200 frames and subsequently summarized. Higher *C* values at specific angles indicate stronger angular correlations in the diffraction pattern and corresponding rotational symmetry of the crystal structure of solidified grains.

1.7 Molecular dynamics simulation

A heating simulation was performed using the molecular dynamics (MD) package *LAMMPS*[49]. A large crystalline model containing 864000 atoms was constructed from an initial FCC lattice. Three compositions were examined: pure Ni, $Ni_{59}Fe_{19}Cr_{22}$ to approximate IN718 alloy, and $Ni_{11.4}Fe_{69}Cr_{19.6}$ to approximate 316L stainless steel. Trace elements were excluded due to the lack of suitable interatomic potentials for covering all minor alloying species. Interatomic potentials among Fe, Cr, and Ni were described using the embedded-atom method (EAM)[50], with the applied Fe-Cr-Ni potential developed by Bonny et. al[51]. Simulations employed a Nose-Hoover

isothermal-isobaric (NPT) algorithm, with pressure fixed at 1 bar and target temperatures of 2000 K and 2300 K. The NPT melting process was applied for 400000 timesteps of 1 fs each, with data collected every 100 timesteps. Simulated data were analyzed in *OVITO*[52], using coordination analysis to compute the pair distribution function *g(r)*. The final simulation frame was used to calculate the 1D *g(r)* profile, which was then converted to the reduced PDF *G(r)* via $G(r) = 4\pi\rho_0[g(r) - 1]$, where ρ_0 is the atomic density of the material. The resulting *G(r)* profiles were compared with experimental measurements.

1.8 Multiphysics computational fluid dynamics simulation

The multiphysics simulation integrating dynamic laser absorption and computational fluid dynamics (CFD) was conducted to evaluate the thermal conditions and melt flow within the melt pool during wire-laser DED of Inconel 718. The commercial software *Flow-3D* (Flow Science Inc., USA) with the AM module was utilized to reconstruct the printing process. The model solved governing equations for multiple fields, including velocity, pressure, volume-of-fluid advection, and conservation of energy, momentum, and mass. Detailed governing equations are described in our previous work[38]. Critical physical phenomena considered in the simulation included phase transformations, gravity, Marangoni convection and surface tension, thermal conduction, laser-matter interactions, laminar turbulence, and viscosity effects.

The geometric configurations of the laser beams, as well as the dimensions of the wire feedstock and substrate, were identical to those employed experimentally. The specific model is illustrated in Fig. S3. As demonstrated in our previous work[38], this model was rigorously validated for wire-laser DED of Inconel 718 through the incorporation of key temperature-dependent material properties. In the present study, to replicate the '*Transitional-R'* printing condition characterized by partial wire melting, we introduced an 'Additional phantom' volume within the melt pool (Fig. S3 and Fig. 4a in the main text). This function applied an additional velocity to the unmelted wire, forcing it to move toward the rear of the melt pool.

A universal mesh size of 0.15 mm was applied across the entire simulation volume, complemented by a finer mesh of 0.075 mm within the melt pool region. The simulation encompassed the printing of an 18 mm line track, using a time step of 0.005 s. These parameters were determined to effectively balance computational accuracy and efficiency.

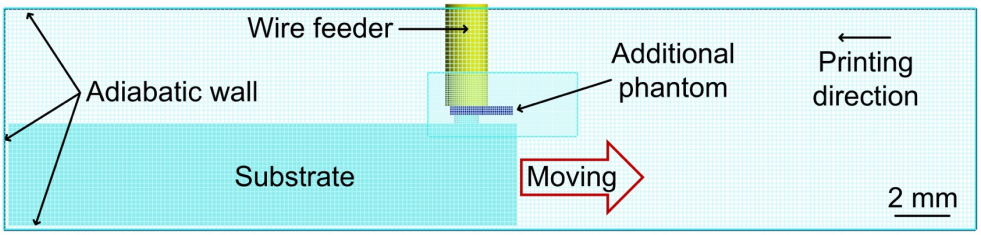

Fig. S3. Multiphysics model of wire-laser DED process. The "Wire feeder" and "Additional phantom" modules apply constant motions to the solid phase within the defined volume, while the substrate moves in the opposite direction of printing. A coarser mesh is used across the global model to capture the overall thermal history, whereas a refined mesh covering the melt pool is employed to resolve the complex melt pool dynamics more accurately. Adiabatic conditions were applied to all boundaries of the model.

2. Supplementary Text

2.1 Visualization of atomic clusters in MD model and partial PDF

Given the strong agreement between the PDF profiles obtained from MD simulations and *operando* synchrotron measurements (Fig. 4d in the main text), we conducted a post-simulation structural analysis to verify the existence of IMRO and FCC-MRO structures in the liquid alloy. Starting from the ideal configurations of icosahedral and FCC-MRO motifs (Fig. 2E), we computed the distance of each atom to the geometrical central atom and determined the number of atoms located at characteristic radial distances. In the final frame of the MD simulation trajectory, 10,000 atoms were randomly selected as central atoms, and their neighboring environments were compared with theoretical radial distances for the two ordering types. To account for the liquid-phase nature of these structures, we applied relaxed tolerances: ±20% for radial distances relative to the theoretical structure and ±50% for coordination numbers in specific shells. Under these criteria, we yielded 49 loosely defined IMRO clusters and 39 loosely defined FCC-MRO clusters in the simulation cell. Their spatial distribution and representative configurations are shown in Fig. S4.

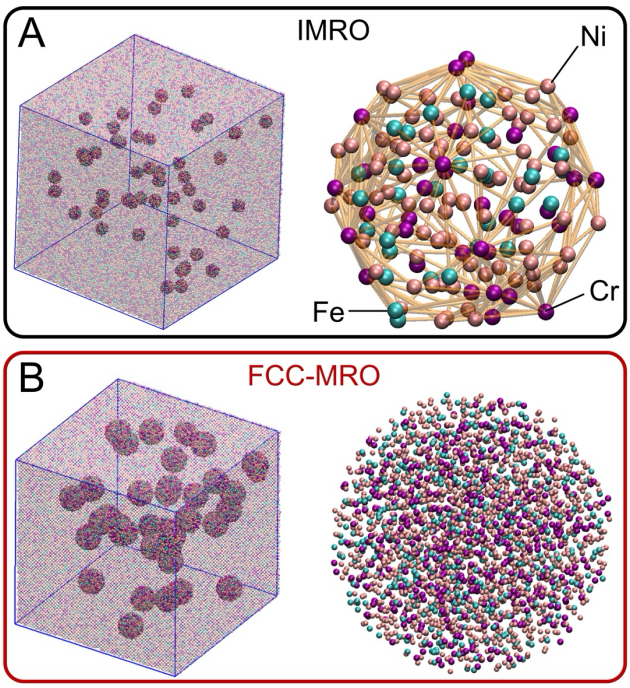

Fig. S4. Visualization of IMRO and FCC-MRO clusters in the MD simulation of liquid Inconel 718 at 2000 K. The left panels show the spatial distribution of **(A)** IMRO and (B) FCC-MRO clusters within the simulation cell. The right panels are two representative atomic models extracted from the simulation cell. Pink, cyan, and purple spheres denote Ni, Fe, and Cr atoms, respectively, as indicated in (**A**). Interatomic bonding is not shown in (**B**) for better clarity.

We extracted the partial PDF, $g(r)$, from the MD result, as shown in Fig. S5. All atomic pairs exhibited a prominent peak at the nearest-neighbor distance with only slight intensity variations, indicating a low tendency for chemical ordering within both MROs in the liquid metal. However, the second primary peak of $g_{Ni\text{-}Cr}(r)$ was shifted towards higher r, which suggests preferential pairing on the higher shells of the IMRO motif. Regarding the influence of minor elements such

as Mo and Nb, their presence should not significantly affect the liquid structure, as indicated by the good agreement between the measured PDF and the simulated result including only the principal elements. Nevertheless, these minor elements may play a more critical role during solidification, thereby influencing the onset of abnormal CET, for example, by hindering or promoting ordering-mediated pathways. The detailed effects of these minor elements require further investigation.

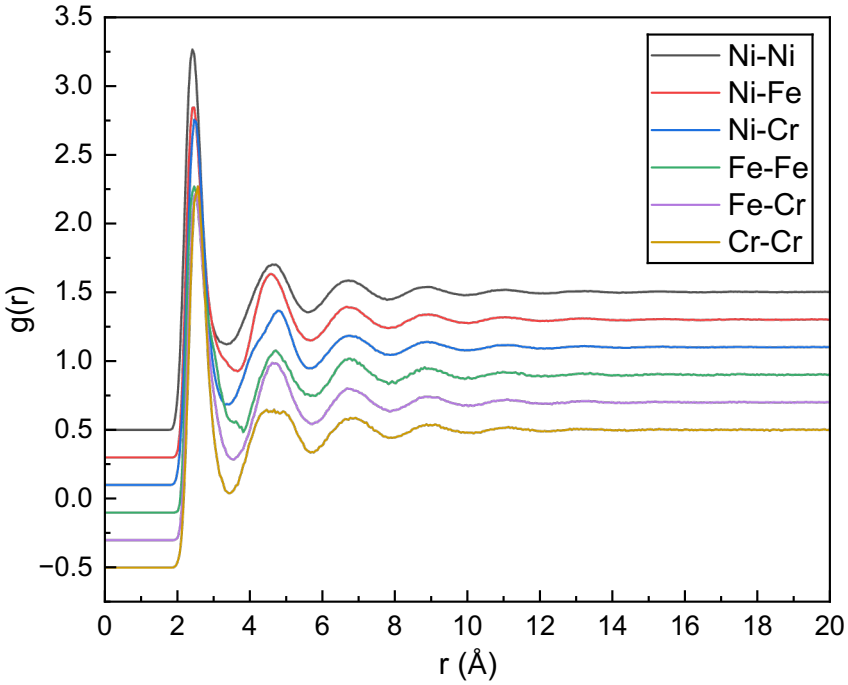

Fig. S5. Partial PDF calculated based on MD simulation of liquid Inconel 718 at 2000 K. The profiles are vertically offset by 0.2 for clarity.

2.2 Influence of deposition direction on printing behavior in coaxial wire-laser DED with triple-laser configuration

As illustrated in Fig. S1B, the melt track deposition in the *operando* synchrotron experiment could be performed by translating the build platform along two opposite directions, denoted as positive ("+") and negative ("–"). Because the μPrinter employs only three laser sources, the coaxial wire-laser configuration inherently introduces anisotropy, resulting in distinct printing behaviors along the "+" and "–" directions.

These differences are illustrated in Fig. S6, which shows the melt pool top surfaces under the two configurations. The geometry of the mushy zone is strongly governed by the laser distribution relative to the rear side of the melt pool. In the "+" configuration, a single laser beam is positioned at the rear side, leading to the formation of a concave mushy-zone surface. This arises from intense localized heating at the melt pool center, accompanied by comparatively rapid cooling at its edges. Such behavior is commonly observed in fusion-based AM processes, and thereby, this configuration has been adopted in all of our previous μPrinter studies[17,38].

In contrast, for the "–" configuration, two laser beams are positioned behind the wire, distributed laterally on both sides of the rear melt pool. In this case, heat absorption is concentrated at the lateral edges, while the central region of the melt pool remains relatively cooler. This effect

is particularly pronounced at lower energy densities, where the morphology of the mushy zone becomes more sensitive to the spatial distribution of laser input.

We employed the "–" deposition direction in our *operando* synchrotron experiment for two reasons: (1) abnormal CET microstructure presents in samples processed under the negative deposition directions, i.e., *Transitional-R*; and (2) the "–" configuration promoted earlier solidification at the melt pool center (where abnormal CET occurred) compared to the lateral surfaces (dominated by coarse columnar grains). This configuration, therefore, provided a more suitable condition for characterizing the evolution of atomic clusters associated with the abnormal CET phenomenon.

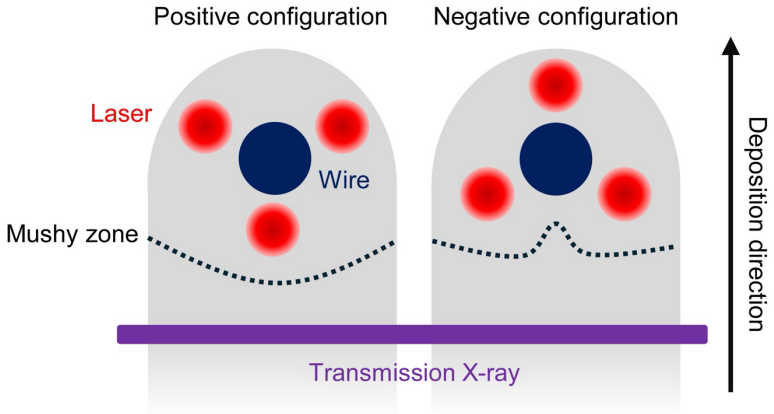

Fig. S6. Schematics of deposition directions in *operando* synchrotron experiment. The left panel shows the positive deposition configuration (+ deposition direction, "*Traditional*" condition), where two laser beams are positioned in front of the wire feedstock and one behind. The synchrotron X-ray beam traverses horizontally across the page, perpendicular to the deposition direction. At this level, the mushy zone exhibits a V-shaped morphology, primarily governed by the laser distribution at the rear side of the melt pool. In contrast, the right panel illustrates the negative deposition configuration (– deposition direction, "*Transitional-R*" condition), where two laser beams are located behind the wire on opposite sides. This arrangement produces a W-shaped mushy zone, which is particularly favorable for synchrotron characterization of the abnormal CET phenomenon.

2.3 Solidification mechanism of the abnormal columnar-to-equiaxed transition and its thermodynamic considerations

As discussed in the main text, direct epitaxial growth is unlikely to occur from IMRO owing to the significant mismatch in atomic configurations between IMRO and FCC crystal. Instead, we propose that the IMRO clusters in the melt pool mediate solidification through the formation of twinned nuclei, as illustrated in Fig. S7. Under localized melt pool conditions with reduced thermal gradient and chaotic melt flow, the decomposition of IMRO initiates, accompanied by the nucleation of twinned embryos. Subsequent epitaxial growth proceeds from these twinned nuclei during solidification.

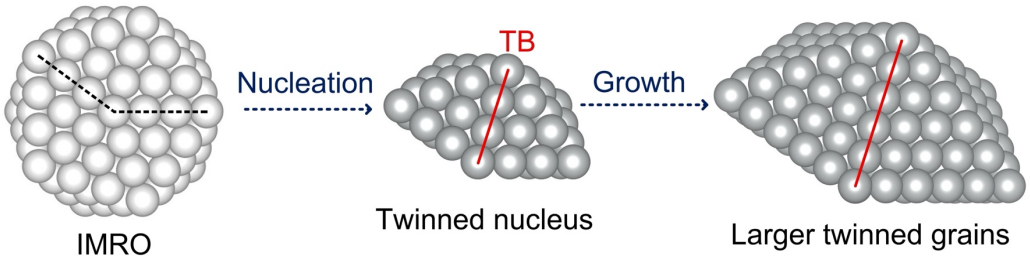

Fig. S7. A schematic illustration of the proposed ordering-mediated solidification mechanism. The red line marks the twinning boundary (TB) within the solid phase, while lighter and darker gray atoms represent the liquid and solid phases, respectively. The process involves the nucleation of a twinned nucleus from a pre-existing IMRO in the melt pool, followed by epitaxial growth leading to the formation of larger twinned grains.

According to the classical nucleation theory, homogeneous nucleation follows the change in Gibbs free energy, $\Delta G(r) = \frac{4\pi}{3} r^3 \Delta G_V + 4\pi r^2 \gamma_{sl}$, where r, ΔG_V, and γ_{sl} denote the nucleus size, volumetric energy change per unit, and the solid-liquid interfacial energy, respectively. The corresponding critical radius r^* is $-2\gamma_{sl}/\Delta G_V$, and the activation barrier ΔG^* is $\frac{16\pi\gamma_{sl}^3}{3\Delta G_V^2}$. For twinned nuclei, however, the change of Gibbs free energy must additionally account for the twin boundary energy (γ_{TB}), assumed as $\Delta G(r) = \frac{4\pi}{3} r^3 \Delta G_V + 4\pi r^2 \gamma_{sl} + \pi r^2 \gamma_{TB}$. Consequently, r^* and ΔG^* increase to $-(2\gamma_{sl} + 0.5\gamma_{TB})/\Delta G_V$, and $\frac{\pi(4\gamma_{sl}+\gamma_{TB})^3}{12\Delta G_V^2}$, respectively. Reported values for Inconel 718 indicate $\gamma_{TB} < 60$ mJ·m^{-2} [53], while the solid-liquid interfacial energy is substantially higher, ~320 mJ·m^{-2} [54]. Based on these estimates, the critical radius r^* and nucleation barrier ΔG^* for twinned nuclei increase by approximately 5% and 15%, respectively. This modest increase suggests that the formation of stable twinned nuclei is thermodynamically feasible. The presence of IMROs in the melt pool, coupled with localized solidification conditions, could thus promote this nucleation pathway.

To obtain further evidence to support the proposed ordering-mediated solidification mechanism involving the formation of twinned nuclei, we performed an MD simulation of the solidification process of $Ni_{59}Fe_{19}Cr_{22}$ (surrogate for Inconel 718). The equilibrium microstructure at 2000 K (Fig. S4) was quenched to 300 K at a constant cooling rate of 2×10^{12} K·s^{-1} under the NPT ensemble. At 858 K, we observed the emergence of a twinned nucleus, as shown in Fig. S8. The highlighted particle exhibiting a twin boundary (red) connecting two FCC grains, analogous to the twinned nucleus sketched in Fig. S7.

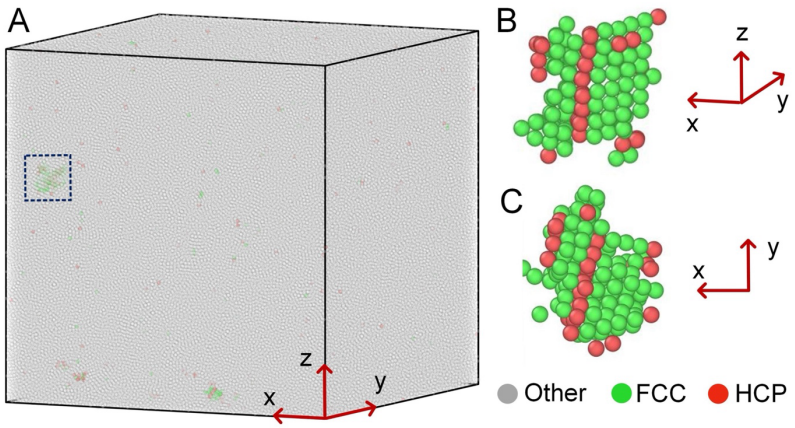

Fig. S8. MD simulation of solidification process of Inconel 718. (**A**) The twinned nucleus in the entire model volume (defined by the black box). (**B-C**) Magnified views of the same twinned nucleus along two different orientations. Atoms outside this particle, whether random or crystallized, are omitted for clarity. This twinned nucleus was identified using common neighbor analysis with a fixed cutoff. The HCP atomic layer (red) marks the twin boundary between the two FCC grains (green).

The above analysis confirmed the possibility of forming twinned nuclei during the solidification of Inconel 718 from two complementary perspectives. A comparable thermodynamic analysis was carried out by Rappaz et al. to assess heterogeneous nucleation on icosahedral quasicrystals[55]. However, it should be noted that general MD simulations can only capture solidification with cooling rates several orders of magnitude faster than our experiments. To avoid over-interpretation, we do not intend to use MD results to explain the entire ordering-mediated mechanism, particularly the transformation from IMRO to twinned nuclei. Such validation will require more advanced computational approaches, including machine-learning-aided MD and exascale supercomputing.

3. Supplementary Figures

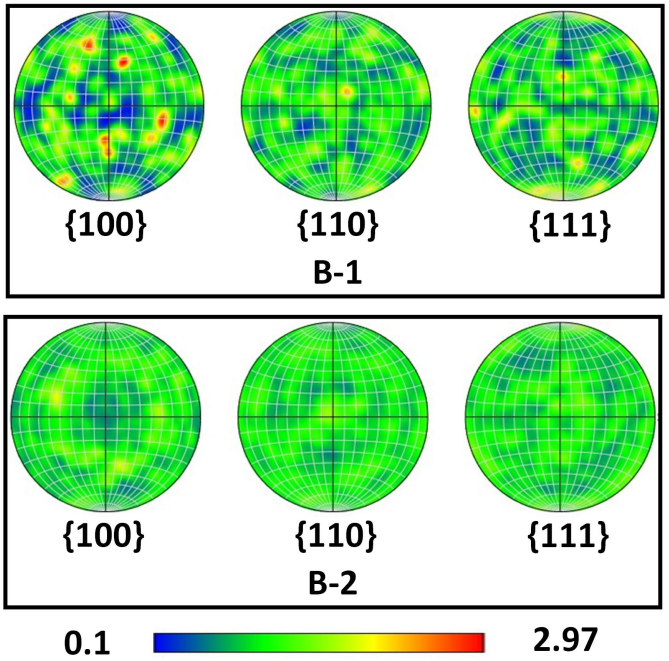

Fig. S9. {100}, {110}, and {111} pole figures for the two regions, B-1 and B-2, of the "*Lack-of-Fusion*" sample shown in Fig. 1 in the main text. The B-1 region presents a stronger crystallographic texture and corresponds to the unmelted wire that remained in the deposited track.

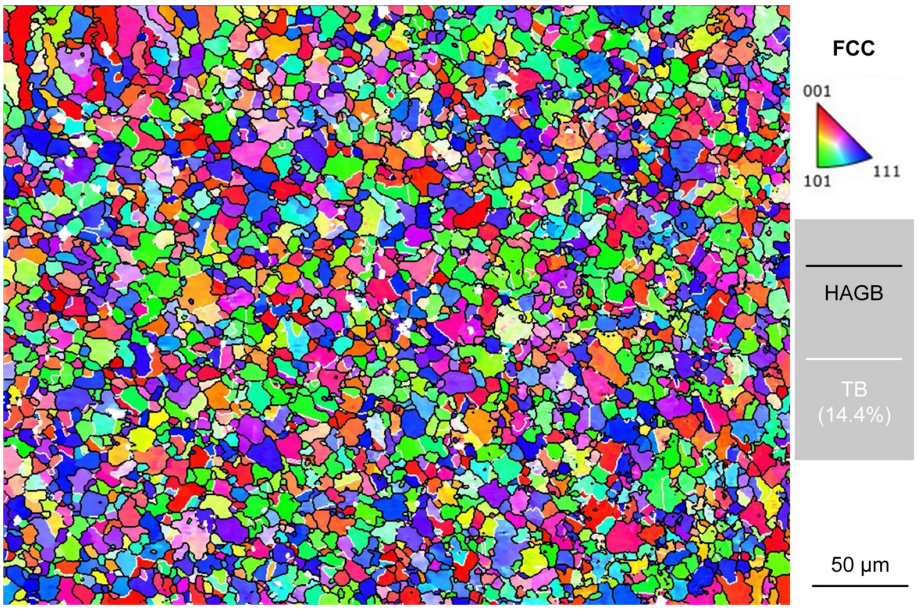

Fig. S10. EBSD-IPF map of the equiaxed grain region in the "*Transitional*" Inconel 718 sample. High-angle grain boundaries (HAGBs) and twin boundaries (TBs) are outlined in black and white, respectively. The fraction of TBs among all boundaries is 14.4%.

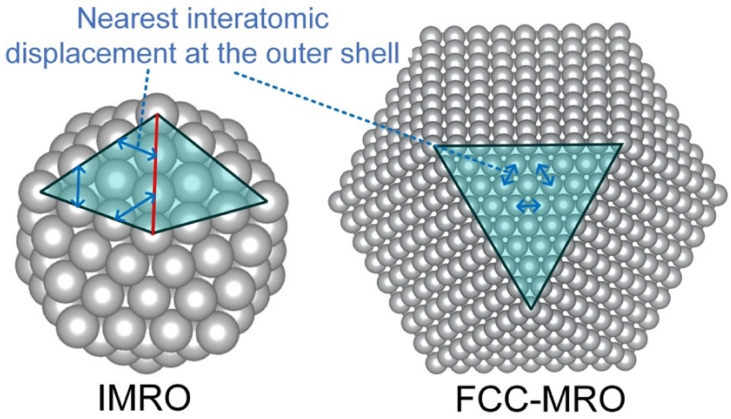

Fig. S11: Illustration of atomic displacement in MRO motifs. The fitted values of the nearest interatomic displacement at the outer shell (marked by blue arrows) are shown in Figs. 3G-3I in the main text.

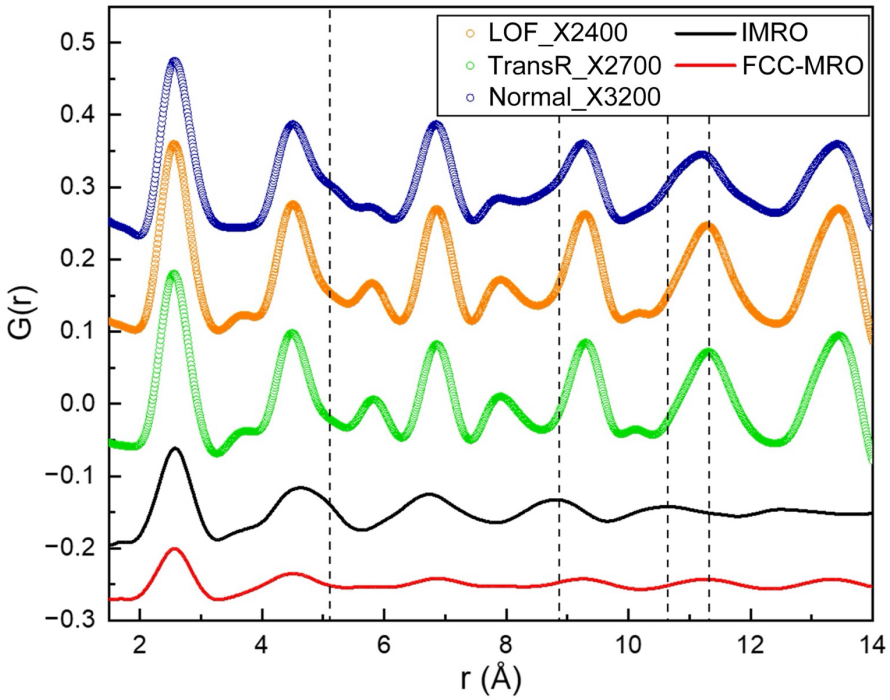

Fig. S12. PDF profiles of the mushy zone under three representative printing conditions: "*Lack-of-fusion (LOF)*", "*Transitional-R (TransR)*", and "*Normal*". The profiles for *LOF*, *TransR*, and *Normal* conditions were collected at X = 2400, 2700, and 3200 mm, respectively. Black and red curves represent fitted PDF components corresponding to IMRO and FCC-MRO in the melt pool of Inconel 718. Three vertical dashed lines highlight peak positions characteristic of IMRO, which appear prominently only under the *Normal* condition. This observation supports the small-box fitting in Fig. 3 in the main text, confirming distinct evolutionary pathways between normal columnar growth and abnormal CET.

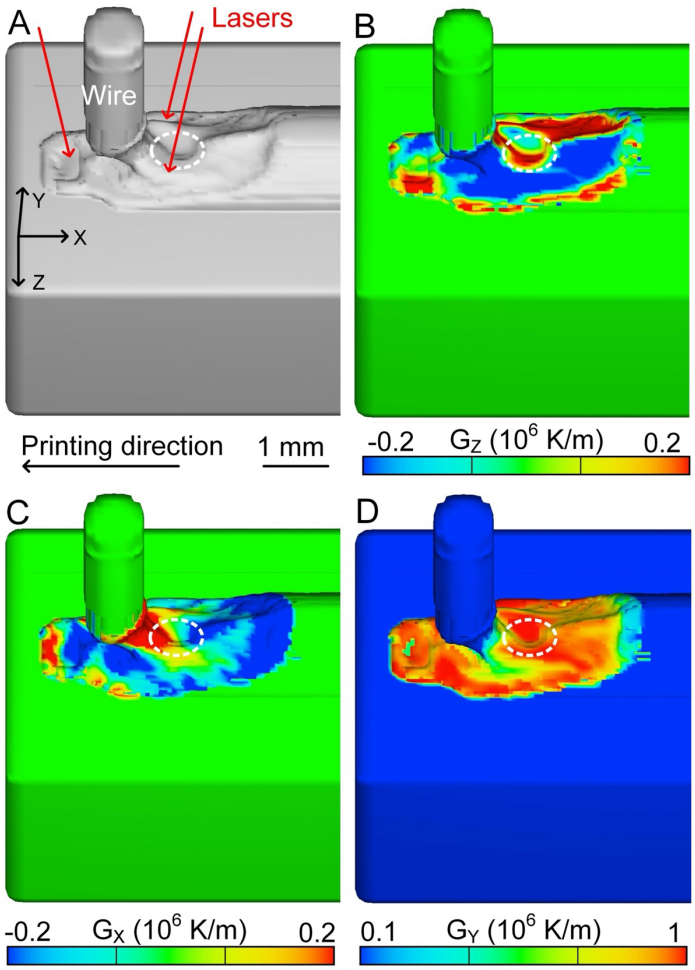

Fig. S13. Multi-physics simulation showing the 3D solidification front and temperature distribution in the melt pool under the "*Transitional-R*" condition. The isosurface of the solidification front is defined by a solid fraction of 0.1. **(A)** 3D contour of the solidification front; corresponding distributions colored by (**B**) G_Z, **(C)** G_X, and **(D)** G_Y. The Y direction is opposite to the feeding direction of the wire. White dashed circles highlight the concave regions in each subfigure, and red arrows in **(A)** mark the approximate positions and directions of the three laser beams.

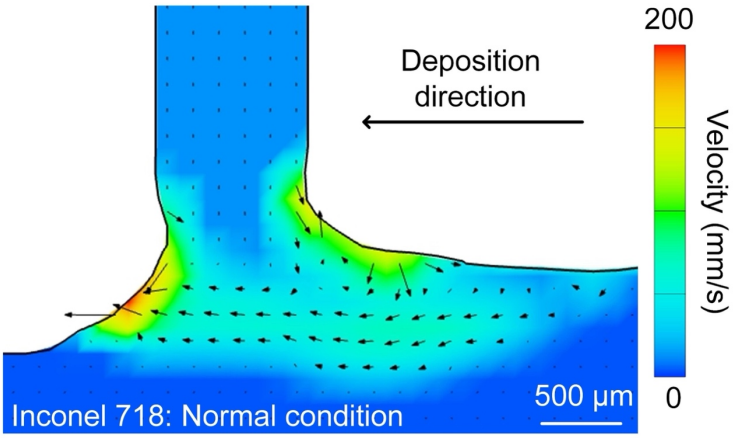

Fig. S14. Multi-physics simulation of melt flow behavior under the "*Normal*" printing condition. This image shows the central plane of the melt pool, with the color scheme representing localized melt flow velocity. This simulation was performed with a uniform mesh size of 0.15 mm and validated as described in our previous work[38]. The absence of a solid wire in the melt pool makes the melt flow behavior less complex than that under the "*Transitional-R*" condition.

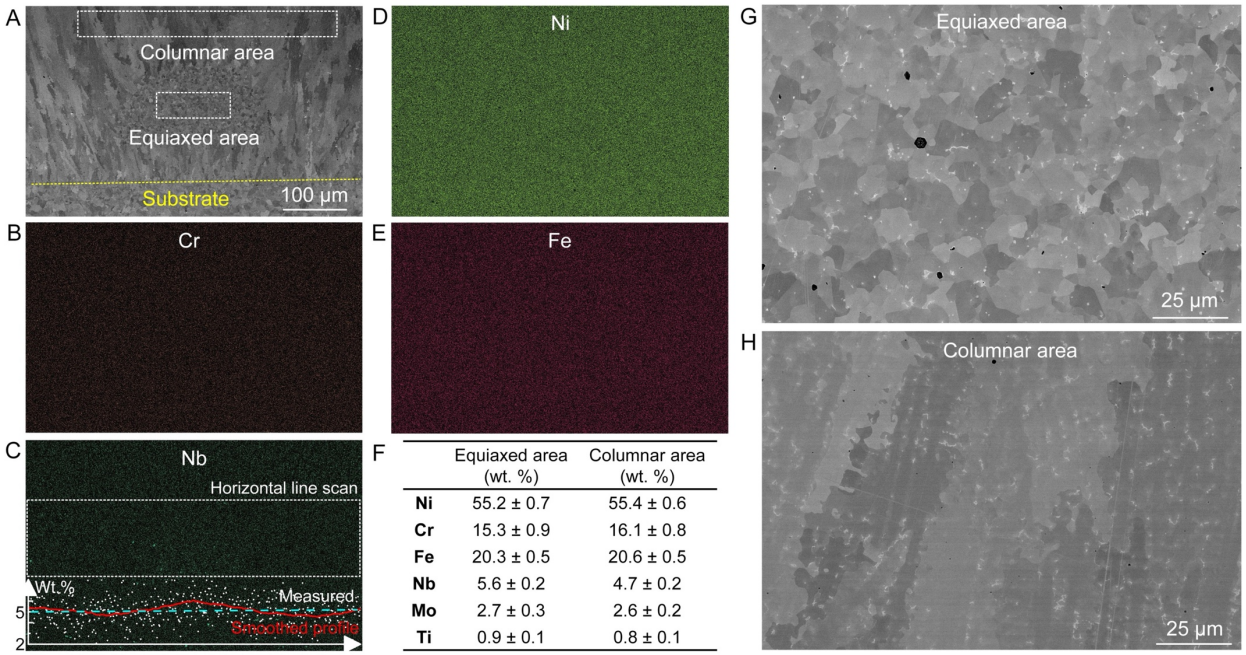

F

	Equiaxed area (wt. %)	Columnar area (wt. %)
Ni	55.2 ± 0.7	55.4 ± 0.6
Cr	15.3 ± 0.9	16.1 ± 0.8
Fe	20.3 ± 0.5	20.6 ± 0.5
Nb	5.6 ± 0.2	4.7 ± 0.2
Mo	2.7 ± 0.3	2.6 ± 0.2
Ti	0.9 ± 0.1	0.8 ± 0.1

Fig. S15. Microstructure of the columnar and equiaxed regions in the Inconel 718 sample built under the "*Transitional*" condition. (A) SEM image of the wire-laser DED single-track sample and **(B-E)** corresponding EDS maps. A horizontal line scan was performed across the area marked in (**C**), with the measured data as white dots and the smoothed profile as a red curve. The cyan dashed line indicates a 5 wt.% reference for comparison. (**F**) Statistical composition measurements at the two marked areas in **(A)**, showing a slightly higher Nb concentration in the equiaxed region than in the columnar region. Magnified SEM images of the **(G)** equiaxed and **(H)** columnar regions reveal that the Laves phase (brighter contrast) is concentrated at grain boundaries in the equiaxed region, but distributed at both grain boundaries and interdendritic areas in the columnar region. Both regions show comparable Laves phase fractions.